Optics Communications 596 (2025) 132417

Contents lists available at ScienceDirect

Optics Communications

journal homepage: www.elsevier.com/locate/optcom

Fiber Bragg grating pressure sensor based on multi-hinges three-levers structure

Shuhui Wei [a], Qiang Liu [a,*], Chao Ma [a], Jianxin Wang [a], Pengfei Lu [a], Tingting Lv [a], Yudan Sun [b], Jingwei Lv [a], Paul K. Chu [c], Chao Liu [a]

[a] School of Physics and Electronic Engineering, Northeast Petroleum University, Daqing, 163318, China
[b] College of Mechanical and Electrical Engineering, Daqing Normal University, Daqing, 163712, China
[c] Department of Physics, Department of Materials Science and Engineering, and Department of Biomedical Engineering, City University of Hong Kong, Tat Chee Avenue, Hong Kong, Kowloon, China

ARTICLE INFO

Keywords:
Pressure sensor
Fiber Bragg grating
Lever structure
Temperature sensor

ABSTRACT

A novel diaphragm pressure sensor based on multi-hinges three-levers structure is proposed and verified. The multi-hinges three-levers structure effectively amplifies the strain of the diaphragm and transfers to the fiber Bragg grating (FBG) which is pasted on the structure, and then the pressure can be measured by observing the central wavelength shift of FBG. The amplification principle of the three-levers structure is analyzed and optimized using the finite element methods. Then the sensor is manufactured and tested in the experiment. The results indicate that the sensitivity of the sensor reaches 4.37 p.m./kPa in the measurement range of 0–1.5 MPa. Meanwhile, another FBG is employed for monitoring temperature and eliminating the cross-sensitivity between temperature and strain. The temperature sensitivity is 11.09 p.m./°C in the range of 20–80 °C. The designed sensor exhibits higher sensitivity and can measure temperature and pressure simultaneously. It has a potential application prospect in the field of the pressure monitoring of oil and gas pipelines.

1. Introduction

The low-pressure measurement plays a crucial role in industrial production. The conventional electrical sensors struggle to maintain long-term stability under severe electromagnetic interference and corrosive environments. The fiber Bragg grating (FBG) sensors have been adopted as the ideal solution for multi-parameter, high-precision monitoring owing to their advantages such as immunity to electromagnetic interference, corrosion resistance, stable signal transmission, and quasi-distributed measurement capabilities [1]. The common pressure sensing approaches include bellows structure [2–4], thin-walled cylinders [5–7], and metallic diaphragms [8–11], then the sensitization structures is designed to convert pressure to micro-strain of FBG. Among these methods, the diaphragm structures can achieve greater strain output under the same pressure loading, resulting in significant sensitivity enhancement. Therefore, diaphragm-type pressure sensors provide a solution for high-sensitivity pressure monitoring in the complex environment.

In order to realize precise pressure measurement, researchers have developed various sensitivity-enhancement structures. Zhao et al. [12] designed a FBG sensor based on a metallic diaphragm coupled with an L-shaped cantilever beam, which can measure pressure in 0–2 MPa with a sensitivity of 0.258 p.m./kPa. Zhang et al. [13] also proposed a FBG pressure sensor which employed a small-scale diaphragm-cantilever structure, and achieved a sensitivity of 1.186 p.m./kPa in the range of 0–2 MPa. To achieve temperature compensation and sensitivity enhancement, Liu et al. [10] introduced a temperature-compensated pressure sensor integrating a metallic diaphragm with a hinge-lever mechanism, the sensitivity reached 5.227 p.m./kPa in 0–1 MPa. Shu et al. [14] presented a non-intrusive pressure sensor which is fixed to the external wall of a pipeline, the sensitivity is 0.393 p.m./kPa. Wu et al. [15] proposed a sensitivity-enhancement structure using dual strain beams and a pipe clamp, the pressure measurement range and sensitivity are 0–1 MPa and 0.354 p.m./kPa respectively. In addition, Li et al. [16] designed a pressure sensor based on a square diaphragm-force-transmission rod configuration with a sensitivity of 1.89 p.m./kPa in the range of 100–500 kPa. Pan et al. [17] proposed a composite pressure-sensing structure combining a Bourdon tube with a

* Corresponding author.
E-mail address: nepulq@126.com (Q. Liu).

https://doi.org/10.1016/j.optcom.2025.132417
Received 8 July 2025; Received in revised form 11 August 2025; Accepted 2 September 2025
Available online 3 September 2025

cantilever beam. In the smaller pressure range of 0–400 kPa the sensitivity reached 5.578 p.m./kPa. Comparing the above studies, it is noticed that the sensor's measurement range and sensitivity are determined by the sensing structure and the sensitization structure.

This paper designs a diaphragm-type pressure sensor based on a multi-hinges three-levers structure. The multiple hinges are introduced to assist the elastic deformation of the three-levers structure, the sensor's sensitivity is obviously enhanced. The three-levers structure is optimized by the finite element method. Then the sensor is manufactured and tested, the pressure sensitivity reaches 4.37 p.m./kPa in 0–1.5 MPa, and the temperature sensitivity is 11.09 p.m./°C. The sensor can measure temperature and pressure simultaneously.

2. Design and sensing principle

2.1. Principle of FBG

Fiber Bragg grating (FBG) is an optical device which can achieve *narrowband* optical *filtering* by inscribing periodic refractive index grating in the fiber core. It means that a narrowband spectrum which satisfies the Bragg phase-matching condition is reflected as a broadband incident light passes through FBG. The peak wavelength λ_B is expressed as [18–20]:

$$\lambda_B = 2n_{eff}\Lambda \tag{1}$$

where n_{eff} denotes the effective refractive index of the fiber core and Λ is the grating period of the FBG, the Bragg wavelength exhibits an ideal linear dependence on n_{eff} and Λ. As the ambient temperature changes ΔT and the axial strain is ε, the Bragg wavelength shift $\Delta\lambda_B$ is given by Ref. [21]:

$$\frac{\Delta\lambda_B}{\lambda_B} = (1 - P_e)\varepsilon + (\xi_f + \alpha_f)\Delta T \tag{2}$$

where p_e denotes photoelastic coefficient, ζ_f denotes thermo-optic coefficient, and α_f denotes thermal expansion coefficient. Therefore the peak wavelength of FBG is sensitive to strain and temperature [22]. In order to eliminate the cross sensitivity between temperature and strain, the dual FBG configuration is typically employed.

2.2. Design of the structure

The diagram of the designed sensor is presented in Fig. 1. The bottom is a metallic diaphragm with an effective radius R and thickness H. The upper section is the multi-hinge three-levers structure which is welded to the diaphragm. FBG1 is bonded between points A and B for pressure measurement, while FBG2 is bonded to the surface of Rod 3 for temperature measurement. To constrain the sensor's lateral dimension, the diaphragm's effective radius is set to $R = 7.5$ mm. Considering the stability and reliability of the sensitization structure, the wall thickness of $b = 1$ mm is adopted. Furthermore, this multi-hinges design can mitigate excessive stress concentration, thereby extend the sensor's life. Detailed dimensions and material parameters of the sensor are provided in Table 1.

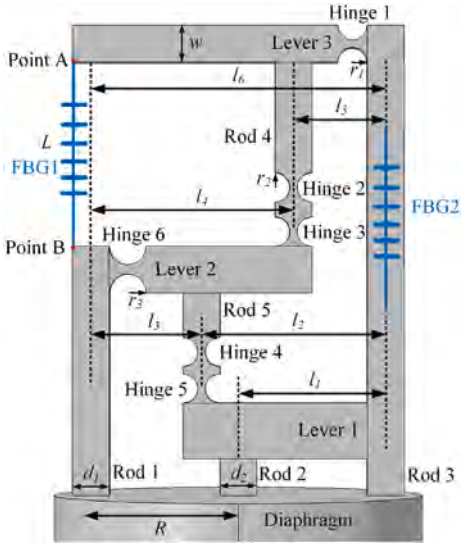

Fig. 1. Diagram of the multi-hinges three-levers structure.

The force analysis of the multi-hinges three-levers structure is depicted in Fig. 2. When the diaphragm is subjected to pressure, the maximum load occurs at the center of the diaphragm, which drives Rod 2 and causes deformation of the multi-hinges three-levers structure. Due to the inherent stiffness of the structure, diaphragm deformation is impeded, generating interaction forces F_0 and F_1. Under the action of the force F_1, Lever 1 rotates clockwise by an angle θ_1 around the pivot point. Due to the force equilibrium, the left end produces a downward balancing force F_2, which is equal in magnitude and opposite in direction with the force F_3. The F_3 drives Lever 2 to rotate counter clockwise by an angle θ_2, and produces a downward balancing force F_4, which is opposite to the force F_5. Finally, Lever 3 rotates clockwise by an angle θ_3 under the force of F_5. The left end of Lever 3 causes axial deformation of the FBG1 and thereby achieves pressure measurement.

Based on the lever principle, the force equilibrium equations for the three levers are derived as follows:

$$F_1 l_1 = F_2 l_2 + K_M \theta_1 \tag{3}$$

$$F_3 l_3 = F_4 l_4 + K_M \theta_2 \tag{4}$$

$$F_2 = F_3 \tag{5}$$

$$F_5 l_5 = k_f x_{out} l_6 + K_M \theta_3 \tag{6}$$

$$F_4 = F_5 \tag{7}$$

where l_i ($i = 1$–6) denote the lengths from the input/output ends of each lever to its pivot, and K_M represents the rotational stiffness of the hinge. The optical fiber is equivalent to a spring, its elastic coefficient k_f and the angles θ_1, θ_2, and θ_3 are expressed as follows:

$$k_f = A_f E_f / L \tag{8}$$

Table 1
Structural parameters of the sensor.

Symbol	Description (units)	Value
R	Effective radius of diaphragm (mm)	7.5
H	Thickness of diaphragm (mm)	0.8
d_1	Width of the Rod 1, Rod3-Rod 5 (mm)	2.0
d_2	Width of the Rod 2 (mm)	2.0
L	Length of Point A to Point B (mm)	10.0
b	Thickness of hinge-lever Structure (mm)	1.0
l_1	Length of Rod 2 to Rod 3 (mm)	8.0
l_2	Length of Rod 5 to Rod 3 (mm)	10.0
l_3	Length of Rod 1 to Rod 5 (mm)	6.0
l_4	Length of Rod 1 to Rod 4 (mm)	11.0
l_5	Length of Rod 4 to Rod 3 (mm)	5.0
l_6	Length of Rod 1 to Rod 3 (mm)	16.0
w	Width of the crossbeam	2.0
r_1	Radius of Hinge 1 (mm)	0.8
r_2	Radius of Hinge 2-Hinge 5 (mm)	0.8
r_3	Radius of Hinge 6 (mm)	1.0
E_f	Young's modulus of optical fiber (GPa)	72
E	Young's modulus of structure (GPa)	200
μ_f	Poisson's ratio of optical fiber	0.23
A_f	Cross-sectional area of the optical fiber (m^2)	1.23×10^{-8}
μ	Poisson's ratio of structure	0.3
ρ	The density of structure (kg/m^3)	8000

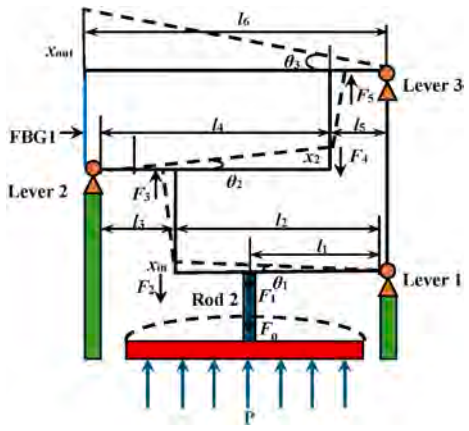

Fig. 2. Force analysis of the multi-hinges three-levers structure.

$$\theta_1 = x_{in}/l_2 \tag{9}$$

$$\theta_2 = x_2/l_4 \tag{10}$$

$$\theta_3 = x_{out}/l_6 \tag{11}$$

where A_f denotes the fiber cross-sectional area, E_f represents the fiber's Young's modulus, and L represents the grating length. Due to the smaller difference for r_1, r_2 and r_3, the radius and waist width of the hinges are uniformly denoted as r and t. Defining $s = r/t$, the rotational stiffness K_M of the hinge is obtained as follows [10]:

$$K_M = \frac{Ebr^2}{12}\left[\frac{2s^3(6s^2+4s+1)}{(2s+1)(4s+1)^2} + \frac{12s^4(2s+1)}{(4s+1)^{5/2}}arctan\sqrt{4s+1}\right]^{-1} \tag{12}$$

By solving the above equations simultaneously, the output displacement x_{out} is obtained as:

$$x_{out} = \frac{L\left(F_1 l_1 l_2 l_3 l_4 l_5 l_6 - K_M x_{in} l_3 l_4 l_5 l_6 - K_M x_2 {l_2}^2 l_5 l_6\right)}{{l_2}^2 {l_4}^2 \left(A_f E_f {l_6}^2 + K_M L\right)} \tag{13}$$

The strain ε of FBG1 can be expressed by the following equation:

$$\varepsilon = x_{out}/L \tag{14}$$

Substituting equations (13) and (14) into (2) and setting $\Delta T = 0$, the wavelength shift of FBG1 is as follows:

$$\frac{\Delta\lambda_B}{\lambda_B} = (1-p_e)\frac{\left(F_1 l_1 l_2 l_3 l_4 l_5 l_6 - K_M x_{in} l_3 l_4 l_5 l_6 - K_M x_2 {l_2}^2 l_5 l_6\right)}{{l_2}^2 {l_4}^2 \left(A_f E_f {l_6}^2 + K_M L\right)} \tag{15}$$

3. Finite element analysis and optimization

To enhance sensor performance, finite element method (FEM) is employed to model the sensor structure and evaluate its mechanical characteristics [23]. The initial structural parameters of the sensor are summarized in Table 1. The material is 304 stainless steel (Young's modulus $E = 200$ GPa, Poisson's ratio $\mu = 0.3$, density $\rho = 8000$ kg/m^3, and thermal expansion coefficient $\alpha = 17 \times 10^{-6}$/°C). Fig. 3(a) shows the mesh division of the structure with a minimum element size of 0.122 mm, so as to ensure precise mechanical engagement at the hinge regions. Then the fixed boundary conditions are imposed along the diaphragm's periphery, an upward pressure load of 1.5 MPa is applied to the effective region of the diaphragm. Considering the yield strength of 304 stainless steel is 205 MPa, an allowable stress of 186 MPa is determined using a safety factor of 1.1. To ensure that the sensor can work stably and overcome long-term creep effects within the range of 0–1.5 MPa for a long time, the maximum stress of the structure must remain below the allowable stress. Fig. 3(b) exhibits the stress distribution of the structure under 1.5 MPa load, the maximum stress of 172 MPa appears at Hinge 3 and is less than the allowable stress. Therefore, the sensor design is reasonable. Fig. 3(c) illustrates the displacement distribution of the sensing structure along the z-axis. As the metallic diaphragm of the base is subjected to pressure, the applied force is transmitted through the three-levers mechanism to the uppermost crossbeam, causing its left end to deflect. By combining this displacement with the experimentally determined strain sensitivity of the FBG, the simulated pressure sensitivity of the sensor can be calculated.

The primary geometric parameters of the sensor are optimized to achieve optimal pressure sensitivity in the range of 0–1.5 MPa. In the optimization process the selected parameter values must ensure that the max stress of the structure is less than the allowable stress of 186 MPa. As the applied pressure is 1.5 MPa, the simulation results are shown in Fig. 4. In Fig. 4 (a) and (c) the gray dashed line represents the allowable stress of the structure. In Fig. 4 (b) and (d) the selected parameters values can ensure that the max stress is less than 186 MPa. Fig. 4(a) shows the influence of diaphragm thickness H on sensor performance. As the thickness H increases, the sensitivity and max stress both decreases.

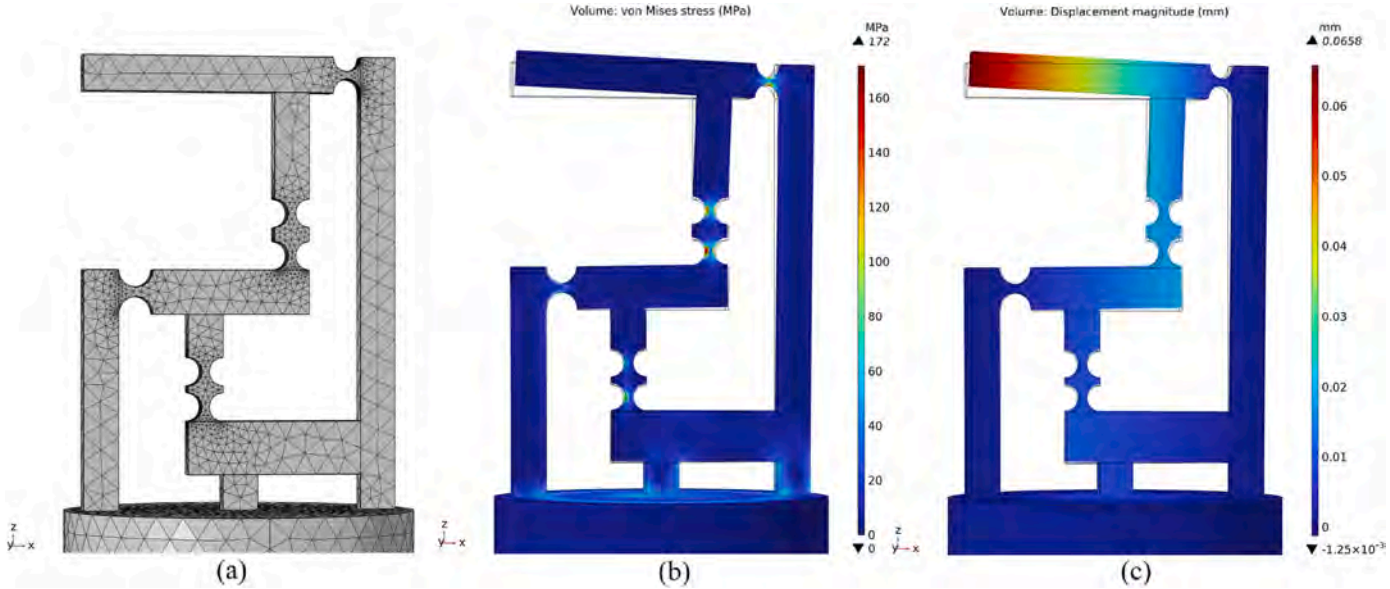

Fig. 3. Sensor simulation (a) mesh division, (b) stress distribution, and (c) displacement distribution.

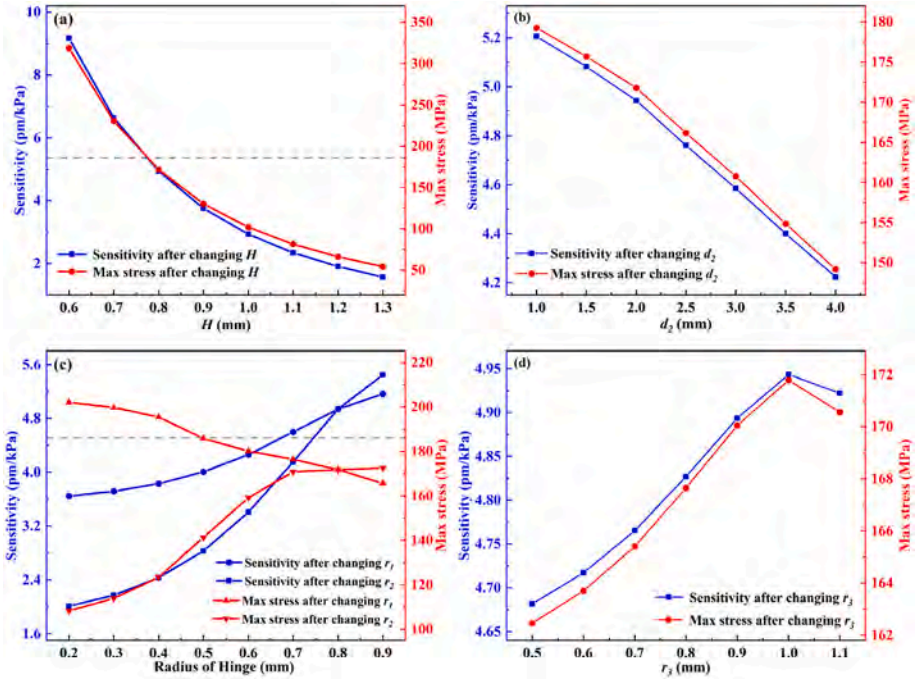

Fig. 4. Effects of sensor parameters on sensitivity and maximum stress (a) diaphragm thickness, (b) width of Rod 2, (c) radius of r_1 and r_2, (d) radius of r_3.

Because a thicker diaphragm undergoes less deformation under the same pressure, which reduces the displacement of Lever 3. Considering the material yield strength and sensitivity, the diaphragm thickness of $H = 0.8$ mm is selected. The effect of the width d_2 is shown in Fig. 4(b). As d_2 increases, the sensitivity and max stress decline. Because a wider Rod 2 increases the contact area with the diaphragm and structural stiffness, thus reduces deformation under the same pressure. In order to get stable structure and higher sensitivity, d_2 is set to 2 mm.

Fig. 4(c) illustrates the influence of hinge radius r_1 and r_2 on sensor performance. As r_1 and r_2 increase, the structure deforms more readily, thereby enhancing sensitivity. Meanwhile, increasing r_1 facilitates the stress distribution and leads to reduction of the maximum stress. Considering fabrication complexity and sensitivity, r_1 and r_2 are set to 0.8 mm. Fig. 4(d) illustrates the effect of radius r_3 on sensor performance. As r_3 increases, the sensitivity and max stress initially rise and then fall. It is because the thinner hinge is not conducive to axial rotation of Lever 2. Therefore, the optimal value *of* r_3 is 1 mm.

Using the optimal structural parameters, the displacements of Point A and Point B are 0.06577 mm and −0.00041 mm respectively. The maximum strain of 6618 με can be calculated as the initial spacing between A and B is $L = 10$ mm. The FBG strain sensitivity of 1.12 p.m./με, the sensor's simulated sensitivity is 4.94 p.m./kPa.

4. Experiments and results

The sensor is fabricated using 304 stainless steel, which has excellent corrosion resistance and can maintain a stable and reliable working condition for a long time in harsh environments. The manufacturing tolerance is ±0.05 mm. The sensor includes two main parts, as shown in the inset of Fig. 5(a). The first part is a hollow cylinder with a metallic diaphragm. The outer threads are used to attach the pressure meter and protective casing. The central part of the sensor is a hexagonal-head bolt. The multi-hinges three-levers structure is welded on the surface of the metal diaphragm. FBG1 with a central wavelength of 1555 nm is pasted between points A and B using 353ND adhesive with a pre-strain of 100 με [24]. Meanwhile, another FBG2 with a central wavelength of 1550

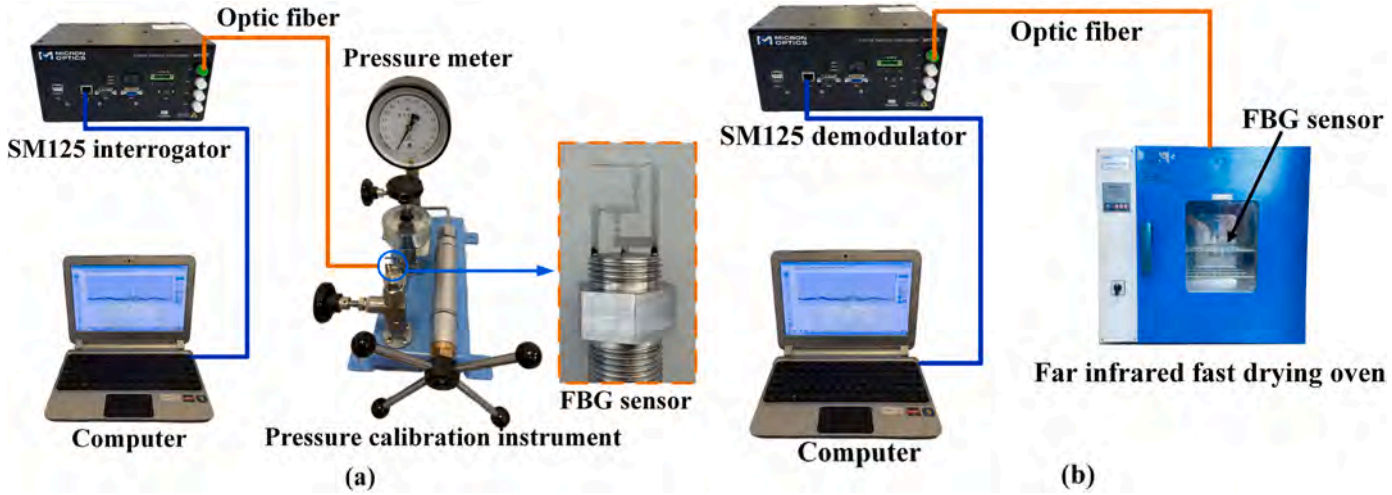

Fig. 5. Test systems: (a) pressure testing; (b) temperature testing.

nm is pasted on the surface of Rod 3 to achieve temperature compensation. After bonding the FBG, the 304 stainless steel casing is installed to protect the inner structure.

As shown in Fig. 5(a), a pressure measurement device is established using a standard pressure meter (0–1.6 MPa, accuracy grade 0.25), the FBG interrogator (MOI SM125, resolution: 1 p.m.) is used to measure reflection spectra of the FBGs. The interrogator is based on tunable Fabry Perot filter technology and can achieve full spectrum scanning. The relationship between pressure and the peak wavelength of FBG1 is measured, thereby achieving the calibration of the FBG pressure sensor. The far-infrared fast drying oven is used to measure the temperature response characteristics of FBG1 and FBG2, as shown in Fig. 5(b).

First, the pressure characteristic is measured at 25 °C. To prevent damage caused by sudden pressure shocks, the pressure is increased from 0.1 MPa to 1.5 MPa in increments of 0.2 MPa, with each pressure level maintained for 20 s. The measured reflection spectra are presented in Fig. 6(a). It is obvious that the reflection spectra of FBG1 shifts toward longer wavelength with increasing pressure and the reflection spectra of FBG2 are unchanged. The relation between the central wavelengths of the two FBGs and pressure are shown in Fig. 6(b). The peak wavelength of FBG1 exhibits a linear trend with pressure, the fitted slope is 4.386 p.m./kPa. The slope of FBG2 is only 0.008 p.m./kPa, indicating its insensitivity to pressure, it is suitable for temperature compensation. Comparing the experimental data and simulation results, the minor difference can attribute to the potential reasons: (1) manufacturing errors of the sensor, (2) The 353ND adhesive decreases the strain transfer efficiency.

To evaluate the repeatability of the sensor, the pressure experiment is repeated four times, as shown in Fig. 7(a). The average pressure sensitivity is 4.37 p.m./kPa with a maximum sensitivity deviation of 0.042 p.m./kPa. The pressure resolution is 228.8 Pa due to the resolution of 1 p.m. for SM125 interrogator. Subsequently, pressure stability tests are performed by maintaining 20 s for each pressure and the result of two loading-unloading cycles is presented in Fig. 7(b). The result confirms that the sensor possesses outstanding stability and rapid response capability.

The temperature characteristics of FBG1 and FBG2 are shown in Fig. 8. The temperature range is between 20 °C and 80 °C with a step of 10 °C, and each temperature is maintained for 20 min. The variations of the central wavelengths of FBG1 and FBG2 exhibit monotonic linear relationship with temperature. The temperature sensitivities of 12.85 p.m./°C for FBG1 and 11.09 p.m./°C for FBG2 are obtained by linear fitting. The results indicate that the temperature significantly affect the response of FBG1. FBG2 can be used for temperature measurement and solve the cross-sensitivity problem of FBG1, thereby achieve simultaneous measurement of pressure and temperature. The measurement method is given in equation (16) [25], S_{T1} and S_{T2} are the temperature sensitivities of FBG1 and FBG2, respectively. S_{P1} and S_{P2} are the pressure sensitivities of FBG1 and FBG2, respectively. As the Bragg wavelengths of FBG1 and FBG2 shift $\Delta\lambda_1$ and $\Delta\lambda_2$, the changes of pressure (ΔP) and temperature (ΔT) can be measured. equation (17) can be deduced by the above obtained sensitivities. Although the sensor can measure temperature and pressure simultaneously, it need be regularly inspected and calibrated to maintain the accuracy of the sensor.

$$\begin{bmatrix}\Delta P\\ \Delta T\end{bmatrix}=\frac{1}{S_{P1}S_{T2}-S_{P2}S_{T1}}\begin{bmatrix}S_{T2} & -S_{T1}\\ -S_{P2} & S_{P1}\end{bmatrix}\begin{bmatrix}\Delta\lambda_1\\ \Delta\lambda_2\end{bmatrix} \tag{16}$$

$$\begin{bmatrix}\Delta P\\ \Delta T\end{bmatrix}=\frac{1}{48.36}\begin{bmatrix}11.09 & -12.85\\ -0.008 & 4.37\end{bmatrix}\begin{bmatrix}\Delta\lambda_1\\ \Delta\lambda_2\end{bmatrix}. \tag{17}$$

Finally, the performance of the proposed sensor is compared with the recently reported FBG-based sensors as shown in Table 2. It is noticed that the sensor of Ref. [10] has the higher sensitivity in the pressure range of 0–1 MPa due to the larger membranes of 10 mm. It increases the size of the sensor. The designed sensor of Ref. [17] exhibits highest sensitivity and narrower measurement range of 0–0.4 MPa. Therefore, the sensitivity and measurement range are mutually constrained and determined by the parameter of the membranes and the sensitization structure. In contrast, our sensor uses a smaller-radius diaphragm and multi-hinges three-levers structure which delivers superior performance. Furthermore, the integrated metallic diaphragm and three-levers structure by welding can provide enhanced long-term stability and reliability. The proposed sensor achieves higher sensitivity in the wider pressure measurement range, the overall performance is superior than any others.

5. Conclusion

This paper presents a diaphragm-type FBG pressure sensor, the sensitivity is enhanced by the novel multi-hinges three-levers structure. The sensitization principle is analyzed and optimized in detail using finite element method. Then the sensor is processed and tested in the experiment. The result shows that the sensor can work stably in the range of 0–1.5 MPa with a sensitivity of 4.37 p.m./kPa. The pressure resolution is 228.8 Pa. Furthermore, the dual-FBG configuration is employed to eliminate cross-sensitivity between temperature and pressure and to measure temperature. The temperature sensitivity is 11.09 p.m./°C. The sensor has the advantages of high sensitivity, wide measurement range and high resolution. It can be used to monitor the pressure of oil and gas pipelines.

CRediT authorship contribution statement

Shuhui Wei: Writing – review & editing, Writing – original draft. **Qiang Liu:** Writing – review & editing, Validation, Supervision, Funding acquisition. **Chao Ma:** Writing – review & editing, Supervision. **Jianxin**

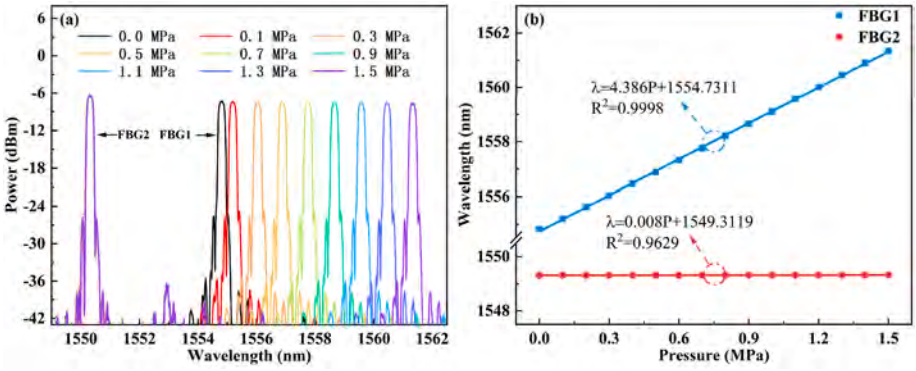

Fig. 6. Reflection spectra and linear fitting results: (a) reflection spectra of the two FBGs; (b) variation of the central wavelengths of the two FBGs with applied pressure.

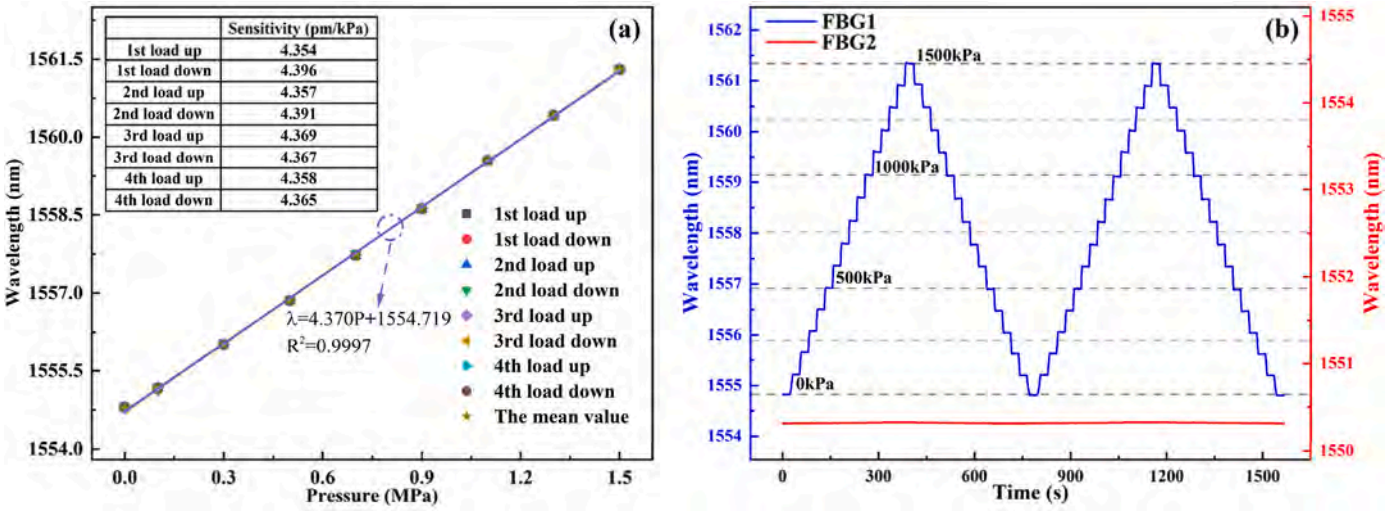

Fig. 7. Repeatability and stability experiments: (a) central wavelength shift of FBG1 versus applied pressure; (b) temporal variation of the central wavelengths of both FBGs.

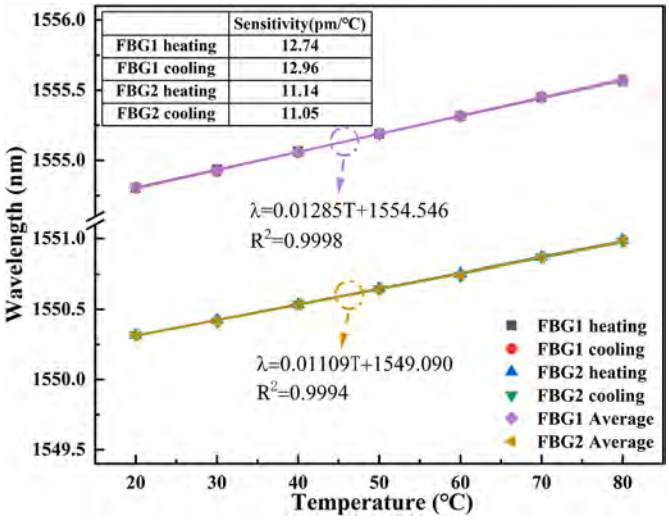

Fig. 8. Variation of the central wavelengths of the two FBGs with temperature.

Table 2
Performance comparison of our sensor with previously reported results.

Ref.	Pressure Range (MPa)	Pressure Sensitivity (pm/kPa)	Temperature Range (°C)
[10]	0–1	5.227	20–80
[12]	0–2	0.258	20–55
[13]	0–2	1.186	NA
[14]	0–1	0.393	NA
[15]	0–1	0.354	NA
[16]	0.1–0.5	1.89	−25-5
[17]	0–0.4	5.578	−10-70
This paper	0–1.5	4.37	20–80

Wang: Supervision. **Pengfei Lu:** Supervision. **Tingting Lv:** Supervision. **Yudan Sun:** Supervision. **Jingwei Lv:** Supervision, Funding acquisition. **Paul K. Chu:** Writing – review & editing, Supervision, Funding acquisition. **Chao Liu:** Writing – review & editing, Supervision, Funding acquisition.

Disclosures

The authors declare no conflicts of interest.

Declaration of competing interest

The manuscript has not been previously published, is not currently submitted for review to any other journal, and will not be submitted elsewhere before a decision is made by this journal.

The authors declare no conflicts of interest.

Acknowledgments

This work was jointly supported by the Basic Research Support Project for the Excellent Youth Scholars of Heilongjiang Province [YQJH2023077], Hainan Province Science and Technology Special Fund [ZDYF2022GXJS222], National Natural Science Foundation of China [12304480], Heilongjiang Provincial Natural Science Foundation of China [JQ2023F001], Local Universities Reformation and Development Personnel Training Supporting Project from Central Authorities, Natural Science Foundation of Heilongjiang Province [LH2021F007], China Postdoctoral Science Foundation funded project [2020M670881], as well as City University of Hong Kong Donation Research Grants [DON-RMG 9229021 and 9220061].

Data availability

Data will be made available on request.

References

[1] D. Xu, D. Feng, Q. Chen, et al., Compact-packaged and diaphragm-lever structured fiber-optic temperature and pressure sensors for oil and gas well applications, IEEE Sens. J. 22 (23) (2022) 22670–22677.
[2] W. Burhanuddin, H. Ahmad, M. Sa'Ad, et al., Fiber bragg grating (FBG)-based pore pressure sensor utilizing bellows system, IEEE Sens. J. 25 (3) (2025) 4706–7414.
[3] P.V. Rao, K. Srimannarayana, M.S. Shankar, et al., High sensitive FBG pressure sensor using metal bellows, Int. Soc. Opt. Eng. 8836 (21) (2013) 10660–10667.
[4] W.L. Yang, Y.L. Xiong, Q.Y. Li, et al., Research on dual bellows FBG pressure sensor, Appl. Mech. Mater. 336 (2013) 239–243.
[5] Y.-F. Gu, Y. Zhao, R.-Q. Lv, et al., A practical FBG sensor based on a thin-walled cylinder for hydraulic pressure measurement, IEEE Photon. Technol. Lett. 28 (22) (2016) 2569–2572.
[6] L. Ji, Q. Sun, S. Zhao, et al., High-resolution fiber grating pressure sensor with in-situ calibration for deep sea exploration, Opt. Express 31 (6) (2023) 10358–10367.
[7] H.-k. Zheng, Y. Zhao, Q. Zhao, et al., High sensitivity optical fiber pressure sensor based on thin-walled oval cylinder, Sensor Actuator Phys. 310 (2020) 112042.

[8] D. Feng, D. Xu, F. Chen, et al., An FBG temperature–pressure sensor based on diaphragm and special-shaped bracket structure, IEEE Sens. J. 23 (4) (2023) 3589–3596.
[9] J. Jing, Y. Guo, T. Wang, et al., A femtosecond fiber bragg grating-based high-sensitivity ocean pressure sensor, IEEE Sens. J. 24 (10) (2024) 16102–16112.
[10] X. Liu, L. Liang, K. Jiang, et al., Sensitivity-enhanced fiber bragg grating pressure sensor based on a diaphragm and hinge-lever structure, IEEE Sens. J. 21 (7) (2021) 9155–9164.
[11] D. Xu, D. Feng, Q. Chen, et al., Small-sized temperature and pressure sensors based on fiber bragg grating for oil and gas wells, Sensor Actuator Phys. 357 (2023) 114397.
[12] Y. Zhao, H.-k. Zheng, R.-q. Lv, et al., A practical FBG pressure sensor based on diaphragm-cantilever, Sensor Actuator Phys. 279 (2018) 101–106.
[13] J. Zhang, L. Liang, K. Mawien, et al., Leak detection of a gathering pipeline based on a sensitive designed fiber bragg grating pressure sensing system, J. Opt. Technol. 90 (6) (2023) 329–335.
[14] Q. Shu, L. Wu, S. Lu, et al., High-sensitivity structure based on fiber bragg grating sensor and its application in nonintrusive detection of pipeline pressure change, Measurement 189 (2022) 110444.
[15] L. Wu, S. Lu, H. Zhang, et al., An FBG-based high-sensitivity structure and its application in non-intrusive detection of pipeline, Measurement 199 (2022) 111498.
[16] L. Zhang, B. Hu, P. Cheng, et al., Design of fiber Bragg grating sensor for static ice pressure detection, Opt. Fiber Technol. 86 (2024) 103845.
[17] J. Pan, F. Xiao, W. Hou, et al., Design and application of pressure sensor based on fiber Bragg grating, Opt. Eng. 63 (3) (2024), 037107-037107.
[18] Q. Liu, B. Li, Y. Sun, et al., FBG demodulation method based on long-period fiber gratings, J. Appl. Opt. 43 (1) (2022) 160.
[19] H. Wang, S. Fan, L. Meng, et al., Multi-parameter sensor based on cascaded multicore FBGs and an FPI for bending, temperature and pressure measurements, Opt Laser. Technol. 175 (2024) 110782.
[20] Q. Liu, S. Wei, S. Gu, et al., High-sensitivity fiber bragg grating pressure sensor with a hinged-lever structure, IEEE Sens. J. 25 (15) (2025) 28314–28322.
[21] Y. Xu, X. Huang, Z. Chen, et al., High-sensitivity optical fiber seawater temperature and pressure sensor with a low-error demodulation method, Opt. Express 33 (2) (2025) 1909–1931.
[22] L. Chen, X. Tong, W. Huang, et al., Highly accurate diaphragm FBG high pressure gas sensor, Opt. Fiber Technol. 84 (2024) 103743.
[23] X. Hu, D. Su, X. Qiao, Diaphragm structured fiber-optic pressure sensors for oil downhole applications, IEEE Sens. J. 24 (9) (2024) 14270–14278.
[24] C. Liu, J. Wang, J. Lv, et al., Economical and easily implemented vernier effect bubble microcavity FPI for strain sensing with extreme low-temperature cross-sensitivity, Infrared Phys. Technol. 150 (2025) 105939.
[25] S. Xu, X. Li, T. Wang, et al., Fiber Bragg grating pressure sensors: a review, Opt. Eng. 62 (1) (2023).